

SwinVFTR: A Novel Volumetric Feature-learning Transformer for 3D OCT Fluid Segmentation

Sharif Amit Kamran¹, Khondker Fariha Hossain¹, Alireza Tavakkoli¹, Stewart Lee Zuckerbrod², Kenton M. Sanders³, and Salah A. Baker³

¹ Dept. of Computer Science & Engineering, University of Nevada, Reno, NV, USA

² School of Medicine, University of Nevada, Reno, NV

³ Houston Eye Associates, Houston, TX

Abstract. Accurately segmenting fluid in 3D volumetric optical coherence tomography (OCT) images is a crucial yet challenging task for detecting eye diseases. Traditional autoencoding-based segmentation approaches have limitations in extracting fluid regions due to successive resolution loss in the encoding phase and the inability to recover lost information in the decoding phase. Although current transformer-based models for medical image segmentation addresses this limitation, they are not designed to be applied out-of-the-box for 3D OCT volumes, which have a wide-ranging channel-axis size based on different vendor device and extraction technique. To address these issues, we propose SwinVFTR, a new transformer-based architecture designed for precise fluid segmentation in 3D volumetric OCT images. We first utilize a channel-wise volumetric sampling for training on OCT volumes with varying depths (B-scans). Next, the model uses a novel shifted window transformer block in the encoder to achieve better localization and segmentation of fluid regions. Additionally, we propose a new volumetric attention block for spatial and depth-wise attention, which improves upon traditional residual skip connections. Consequently, utilizing multi-class dice loss, the proposed architecture outperforms other existing architectures on the three publicly available vendor-specific OCT datasets, namely Spectralis, Cirrus, and Topcon, with mean dice scores of 0.72, 0.59, and 0.68, respectively. Additionally, SwinVFTR outperforms other architectures in two additional relevant metrics, mean intersection-over-union (Mean-IOU) and structural similarity measure (SSIM).

Keywords: Fluid Segmentation · Optical Coherence Tomography · Swin Transformer · OCT Segmentation.

1 Introduction

The macula is part of the retinal subspace primarily responsible for central vision. Fluid buildup, or macular edema in retinal layers, is a common reason for blindness and retinal degeneration [7]. Possible factors include Drusen, Choroidal neovascularization (CNV), Age-related macular degeneration (AMD), and Diabetic retinopathy (DR) [7,26]. Age-related macular degeneration causes irreversible blindness in approximately 8.7% of people worldwide and is a leading cause of vision loss. Furthermore, it is projected to increase threefold each decade for people over 40 in developed countries

[28]. Similarly, Diabetic retinopathy affects one-third of every diabetic patient [25], which is 2.8% of the world’s population and the second leading cause of blindness [2]. As a result, early diagnosis, localization, and segmentation of retinal layer fluid accumulation can help with effective treatments and personalized therapy. Optical coherence tomography (OCT) is a non-invasive retinal imaging method [23] that yields 3D volumetric cross-sectional images for viewing the morphology of retinal layers and underlying pathologies. Although the image is extracted through this approach, the differential diagnosis and fluid localization are supervised by an expert ophthalmologist.

Manual annotation and segmentation of sub-retinal fluid can be time-consuming, subject to error, and tedious task. Hence, experts in the past proposed and incorporated many image-processing [5,6] and machine learning [3,20] techniques to alleviate this problem. However, those traditional approaches required handcrafted feature engineering and pruning, trouble learning spatial and depth features, and less generalization ability. With the advent of deep learning, automated segmentation tasks for medical imaging has surged in popularity, given their effectiveness to pixel-wise segment with high accuracy and precise surface estimation for volumetric and spatial imaging data. For retinal fluid segmentation, 2D U-Net-like auto-encoder models have been predominantly incorporated in early [21,22] and recent works [30,16,29,10]. These models achieved quite good results for multi-layer fluid segmentation in overall metrics. However, these architectures fail when segmenting fine fluid-layer boundaries and detecting small deposits of fluids. In contrast, recent vision transformer-based auto-encoders for fluid segmentation try to address this problem by utilizing multi-headed window attention [27], or shifted-window attention [19] for capturing local context, improving tiny fluid segmentation. The biggest drawback is these approaches are trained and tested on 2D slices, which only contain spatial features and have no context regarding inter-slice depth information. Though an early work [14] has utilized a 3D U-Net model for retinal fluid segmentation, any new development since then has been stagnant.

Our Contributions: By taking all this into account, we propose a novel architecture termed Swin Volumetric Feature-learning Transformer (SwinVFTR) that utilizes a swin-transformer as an encoder and joins it to a 3D convolution-based decoder at distinct resolutions via novel volumetric spatial and depth attention block. Moreover, we modify the swin-transformer block with a Multi-receptive field residual block instead of MLP. Our model employs a channel-wise overlapped sampling technique to crop OCT volumes only in the depth axis, while retaining the spatial information. To validate our work, we compare four different 3D convolution and transformer-based architectures for medical image segmentation on three vendor-specific OCT datasets: Spectralis, Cirrus, and Topcon [1]. From Fig. 2, it is apparent that our architecture segments retinal fluid with high dice-score and mean-IOU.

2 SwinVFTR

2.1 Channel-wise Volumetric Sampling

Sampling OCT B-scans at different depths can affect the outcome of recognizing retinal disease pathology for accurate diagnosis [17]. Although U-Net-like architectures

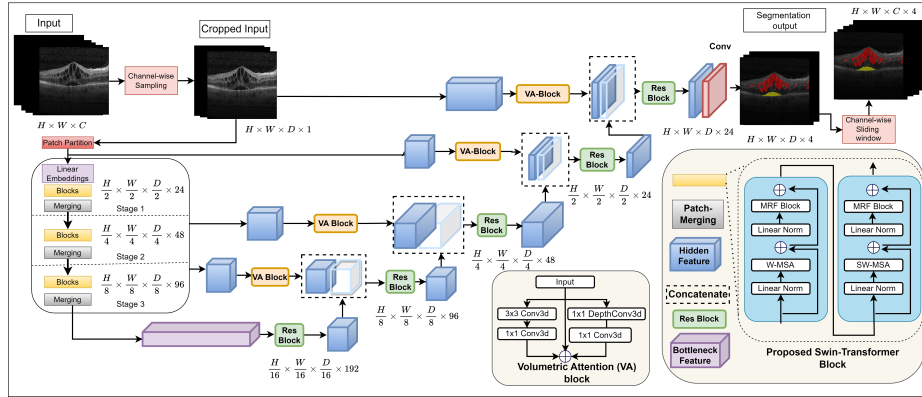


Fig. 1: Proposed SwinVFTR architecture which takes 3D OCT volume input with channel-wise sampling technique and outputs a 3D segmentation map of the fluid accumulation. The SwinVFTR encoder incorporates a new swin-transformer block consisting of Shifted window attention, Multi-headed attention and Multi-Receptive Field (MRF) sub-block with both convolution and dilated convolution layers. The encoder features are sequentially added with the decoder using a skip-connection consisting of a volumetric attention (VA) block.

are flexible in handling OCT volumes of different depths, current transformer-based architecture cannot take OCTs with smaller depths. For example, UNETR [9] and Swin-UNETR [8], two state-of-the-art models for medical image segmentation, utilize patch-merging layer to downsample $\times 32$. As a result, any OCT with less than 64 B-scans cannot be used out-of-the-box for these models. Since we are working on diversified OCT volumes with B-scans of 49 to 128, utilizing volumetric cropping would be ideal. However, we want to retain the spatial information while sampling a section of the original B-scans. So we introduce a channel-wise sampling technique that samples a $H \times W \times D$ dimensional cropped image from an image with $H \times W \times C$ dimensions, where $D < C$ and $D = 32$. We also utilize one less swin-transformer and patch-merging block to make our downsampling $\times 16$. While producing the output, we do channel-wise overlapped volume stitching (25% overlap) which is given in Fig. 1.

2.2 Proposed Swin-Transformer Block

Regular window-based multi-head self-attention (W-MSA), which was incorporated in Vision Transformer (ViT) [4], employs a single low-resolution window for constructing a global feature map and has quadratic computation complexity. Contrastly, the Swin Transformer architecture proposed in [15] integrates shifted windows multi-head self-attention (SW-MSA), which builds hierarchical local feature maps and has linear computation complexity. Recently, Swin-UNETR [8] adopted this swin-transformer block without making any fundamental changes and achieved state-of-the-art dice scores in different 3D medical image segmentation tasks. One of the most significant drawback of

these blocks is using a Multi-layer perceptron block (MLP) after the post-normalization layer. MLP utilizes two linear (dense) layers, which are computationally more expensive than a 1D convolution with a small kernel. For example, a linear embedding output from a swin-transformer layer having dimension X (where $X = H \times W \times D$), and input channel, C_{in} and output channel, C_{out} will have a total number of parameters, $X \times C_{in} \times C_{out}$. In contrast, a 1D Conv with kernel size, k with the same input and output will have less number of parameters, $k \times C_{in} \times C_{out}$. Here, we did not consider any parameters for bias and the value of $k = \{1, 3\}$. On the other hand, using 1D convolution will drastically affect the performance, given that small receptive fields only accounts for local features and not global ones. Hence, we employ a multi-branch residual block with vanilla and dilated convolution termed, Multi-receptive field Block (MRF) to address this. So for subsequent layers, l and $l + 1$, the proposed swin-transformer block can be defined as Eq. 1.

$$\begin{aligned}
 d^l &= W\text{-MSA}(\psi(d^{l-1})) \\
 d^l &= MRF(\psi(d^l)) + d^l \\
 d^{l+1} &= SW\text{-MSA}(\sigma(d^l)) \\
 d^{l+1} &= MRF(\psi(d^{l+1})) + d^{l+1}
 \end{aligned} \tag{1}$$

In Eq. 1, we visualize the first sub-block of swin-transformer consisting of Layer-Norm (ψ) layer, multi-head self attention module (W-MSA), residual connection (+) and Multi-receptive field block (MRF). In a similar manner, the second sub-block of swin transformer consisting of LayerNorm (ψ) layer, shifted window multi-head self attention module (SW-MSA), residual skip-connection (+) and Multi-receptive field block (MRF). Moreover, l signifies the layer number and d is the feature-map. The MRF block can be further elaborated as given in Eq. 2.

$$\begin{aligned}
 x^1 &= \delta(\text{Conv}(x_{in})) \\
 x^2 &= \delta(\text{Depthwise_Conv}(x^1)) \\
 x^3 &= \delta(\text{Dilated_Conv}(x_{in})) \\
 x_{out} &= \delta(\text{Conv}(x^1 + x^2 + x^3))
 \end{aligned} \tag{2}$$

In Eq. 2, we first use convolution with kernel size, $k = 1$, and stride, $s = 1$ to extract local features with a small receptive field. Then, the output of these layers is inserted into a depth-wise convolution layer ($k = 1, s = 1$). In a parallel branch, a dilated convolution ($k = 3, s = 1$) with dilation rate, $d = 2$ is utilized to extract features with a larger receptive field. Finally, we add all these outputs from these three convolution layers and then apply a convolution ($k = 1, s = 1$) to get the final result. Here, δ signifies the GELU activation, which is applied to all convolution layers.

2.3 Encoder

Before the encoder can take the input with dimensions $H \times W \times D$, we transform the OCT volumetric images. We employ a patch partition step to create a sequence of 3D

tokens with a dimension of $\frac{H}{P} \times \frac{W}{P} \times \frac{D}{P}$ and these features are then projected to an embedding space with dimension C . Specifically, our encoder has a non-overlapping patch with a size of $2 \times 2 \times 2$ and a feature dimension of $2 \times 2 \times 2 \times 1 = 16$ by considering one channel of the OCT. We assign the embedding space size, $C=24$, in our encoder. So the feature output of the patch-partition layer is $\frac{H}{2} \times \frac{W}{2} \times \frac{D}{2} \times 24$. Likewise, each encoder stage downsamples the features by utilizing two swin-transformer blocks followed by a patch-merging block. So, the features size changes from $\frac{H}{2} \times \frac{W}{2} \times \frac{D}{2} \times C$ to $\frac{H}{4} \times \frac{W}{4} \times \frac{D}{4} \times 2C$, from $\frac{H}{4} \times \frac{W}{4} \times \frac{D}{4} \times 2C$ to $\frac{H}{8} \times \frac{W}{8} \times \frac{D}{8} \times 4C$, and from $\frac{H}{8} \times \frac{W}{8} \times \frac{D}{8} \times 4C$ to $\frac{H}{16} \times \frac{W}{16} \times \frac{D}{16} \times 8C$, successively. We incorporate two swin-transformer blocks after the last patch-merging layer to finalize the encoder.

2.4 Volumetric Attention Block

In 3D UNet-like architectures [9,14,13], skip connections concatenate the encoder and decoder features to retain loss of information. However, to make these features more robust, Swin-UNETR incorporated residual attention block with two convolution layers similar to [18,11]. The problem with this approach is that it utilizes regular convolution, which only applies attention spatially and ignores any channel-wise attention. To alleviate this, we propose a volumetric attention (VA) block consisting of separate branches. In the first branch, we have a $3 \times 3 \times 3$ followed by a $1 \times 1 \times 1$ convolution for spatial attention. In the following branch, we have a $1 \times 1 \times 1$ depth-wise convolution followed by a $1 \times 1 \times 1$ point-wise convolution for channel-wise attention. In the final branch, we have an identity function that copies the input features. Consequently, we add all of these features to generate our last output feature.

2.5 Decoder

Similar to our encoder, we design a symmetric decoder composed of multiple transposed convolution blocks and a volumetric concatenation layer between each stage of the encoder and decoder features. At each stage n ($n \in 1, 2, 3$) in the encoder and bottleneck ($n = 4$), the volumetric feature representations are reshaped to $\frac{H}{2^n} \times \frac{H}{2^n} \times \frac{H}{2^n}$ and inserted into a residual convolution block with with two $3 \times 3 \times 3$ convolution followed by instance normalization layer. Each decoder's feature maps are doubled in size using a transposed convolution layer. Moreover, each encoder's skip feature maps through the VA blocks are concatenated with the outputs of the previous decoder. Finally, a residual convolution block is applied to the feature with two $3 \times 3 \times 3$ convolutions followed by an instance normalization layer. The final segmentation output is generated using a $1 \times 1 \times 1$ convolutional layer and a softmax activation function.

2.6 Objective Function

For our segmentation output we utilize the Dice coefficient loss given in Eq. 3. For dice-coefficient we use $\epsilon = 1.0$ in numerator and denominator for addressing the division by zero. Here, \mathbb{E} signifies, expected values given, y' (prediction) and y (ground-truth).

$$\mathcal{L}_{dice} = \mathbb{E}_{y',y} \left[1 - \frac{2 \sum_{i=1}^N y'_i y_i + \epsilon}{\sum_{i=1}^N y'_i + \sum_{i=1}^N y_i + \epsilon} \right] \quad (3)$$

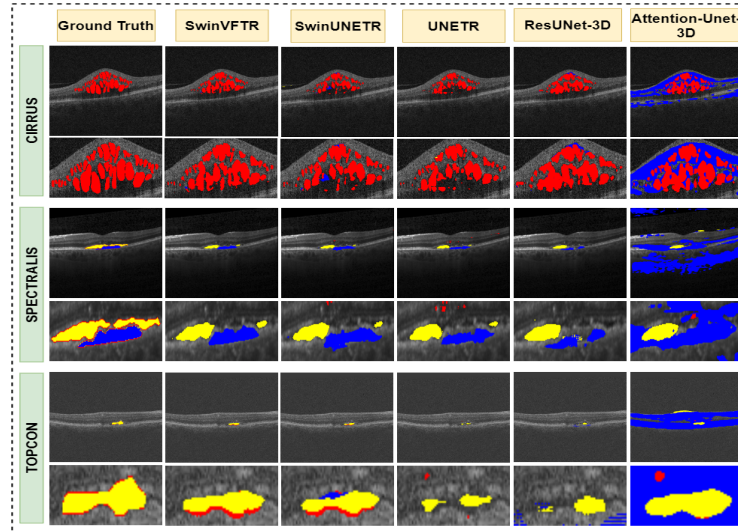


Fig. 2: SwinVFTR segments fluid with better precision than other 3D CNN and Transformer architectures. The row contains Cirrus, Spectralis and Topcon data-sets. Whereas the column contains ground-truths and segmentation maps for SwinVFTR, SwinUNETR, UNETR, ResUNet-3D and Attention-UNet-3D. Here, IRF, SRF, and PED fluids are colored as Red, Yellow and Blue.

3 Experiments

3.1 Dataset and Preprocessing

For benchmarking, we use the RETOUCH public dataset [1], which contains three image sets from three unique vendor devices and, in total, has 70 volumes. Out of this, 24 volumes were obtained with Cirrus (Zeiss), 24 volumes with Spectralis (Heidelberg), and 22 volumes with T-1000 and T-2000 (Topcon) devices. The numbers of B-scans (volume depths) were 128, 49, and 128, with resolutions of 512×1024 , 512×496 , and 512×885 , respectively, for each of these vendor devices. We only resize Cirrus and Topcon volumes to 512×512 resolution. The volume contained three different fluids such as intra-retinal fluid (IRF), sub-retinal fluid (SRF), and pigment epithelial detachment (PED), which were manually annotated by an expert as separate ground truth volumes. As test datasets are no more publicly available, we separate the original image sets into training and test set. So for Cirrus and Spectralis, we had 19 training and 5 test volumes, whereas, for Topcon, we had 18 training and 4 test volumes. We further utilize 5-fold cross-validation to find the model with the highest dice score. For image transformations, we apply Random Intensity Shift (± 10 with 50% probability) and Random Channel-wise volumetric cropping for training our model.

Data use declaration and acknowledgment: The dataset was released as part of Retouch Challenge. For usage, please refer to the data confidentiality agreement.

Table 1: Quantitative comparison on Spectralis, Cirrus, & Topcon [1].

Dataset	Method	Year	SSIM	Mean-IOU	Dice Score			Mean Dice	
					IRF	SRF	PED	w/o BG	w/ BG
Spectralis	Attention-UNet-3D [18]	2018	0.914	0.439	0.608	0.394	0.096	0.366	0.517
	ResUNet-3D[11]	2019	0.985	0.595	0.602	0.574	0.602	0.592	0.694
	UNETR [9]	2022	0.984	0.546	0.567	0.493	0.544	0.534	0.651
	SwinUNETR [8,24]	2022	0.985	0.613	0.601	0.544	0.662	0.602	0.701
	SwinVFTR	2023	0.987	0.625	0.624	0.578	0.670	0.624	0.718
Cirrus	Attention-UNet-3D [18]	2018	0.928	0.446	0.664	0.472	0.011	0.382	0.527
	ResUNet-3D [11]	2019	0.983	0.490	0.648	0.622	0.012	0.427	0.570
	UNETR [9]	2022	0.987	0.487	0.635	0.594	0.081	0.436	0.577
	SwinUNETR [8,24]	2022	0.986	0.452	0.682	0.338	0.131	0.384	0.537
	SwinVFTR	2021	0.988	0.492	0.691	0.507	0.146	0.448	0.587
Topconn	Attention-UNet-3D [18]	2018	0.894	0.412	0.526	0.542	0.083	0.383	0.519
	ResUNet-3D [11]	2019	0.974	0.526	0.534	0.648	0.419	0.534	0.649
	UNETR [9]	2022	0.979	0.495	0.592	0.416	0.427	0.478	0.607
	SwinUNETR [8,24]	2022	0.980	0.483	0.583	0.451	0.331	0.455	0.590
	SwinVFTR	2023	0.981	0.553	0.638	0.523	0.548	0.571	0.678

3.2 Hyper-parameter Initialization

We used Adam optimizer [12], with learning rate $\alpha = 0.0001$, $\beta_1 = 0.9$ and $\beta_2 = 0.999$. We train with mini-batches with batch size, $b = 1$ for 600 epochs using PyTorch and MONAI library monai.io. It took between 8-12 hours to train our model on NVIDIA A30 GPU, depending on the data-set. Because Spectralis has a lower number of B-scans compared to Cirrus and Topcon, it takes less amount to train. The inference time is 0.5 second per volume. We provide ablation for hyper-parameter selections in subsection 3.4 and in the supplementary materials. The code repository is provided in this link.

3.3 Quantitative Evaluation

We compared our architecture with some best-performing 3D CNN and Transformer architectures, including ResUNet-3D [11], AttentionUNet-3D [18], UNETR [9] and SwinUNETR [8] as illustrated in Fig. 2. We trained and evaluated all four architectures using their publicly available source code on the three datasets. SwinUNETR utilizes a swin-transformer encoder as a backbone and a step-wise decoder with transposed convolution and residual blocks to upsample the features. In contrast, the UNETR employs a vision transformer with self-attention layers as encoders and deconvolution layers for upsampling. ResUnet-3D and Attention-UNet-3D are simple modifications of UNet 3D architectures, with the first using residual layers in the encoder and decoders and the second incorporating attention in the skip connections between them. In Fig. 2, we visualize segmentation results for intra-retinal fluid (IRF), sub-retinal fluid (SRF), and pigment epithelium detachments (PED). It is apparent from the figure that our model’s prediction is more accurate than other transformer and CNN-based architectures, and the segmentation boundary is finer and less coarse than SwinUNETR and UNETR.

Next, we quantitatively evaluate all five models using mean-intersection-over-union (mIOU), dice scores, and structural similarity index (SSIM) as shown in Table. 1. We also provide fluid-wise dice scores for IRF, SRF, and PED. Table. 1 shows that our model’s overall dice score, SSIM, and mIOU far exceed other architectures. Although for Cirrus and Topcon, our model’s segmentation performance is a little worse for SRF fluid against ResUNet-3D, the dice score PED is almost $10\times$ better for Cirrus and $1.2\times$ better for Topcon. Another essential evaluation we did was calculating dice score with (w/ BG) and without background (w/o BG), as background contains the majority of the pixels, and it can skew the results with high false-positive rates. As the table shows, our model outperforms other architectures with a higher dice score for both with and without background.

3.4 Ablation Study

Hyper-parameter search: In supplementary Table. 1, we have provided the effects of different hyper-parameters such as epoch e , learning rate, α and batch-size, b . Our search space for epoch, $e = \{100, 300, 600\}$, learning-rate, $\alpha = \{10e-4, 5e-5, 10e-5\}$, and batch-size, $b = \{1, 2, 3\}$. We found $e = 600$, $\alpha = 10e-4$, and $b = 1$ to be the best-performing hyper-parameters for SwinVFTR.

Effects of Architectural Change: In the supplementary Table. 2, we provide the comparative comparison of SwinVFSTR’s performance with and without VA (Volumetric Attention) and MRF (Multi-receptive field) Blocks. As the results show, our model with VA and MRF achieves the highest dice score and mean-IOU, and our model with VA only performs the second best. The model without VA and MRF blocks incorporates residual convolution for skip connected instead of VA and regular swin-transformer layer with MLP instead of MRF.

4 Conclusion

In this paper, we proposed a new 3D transformer-based fluid segmentation architecture called SwinVFTR. Combining our novel channel-wise sampling technique, incorporating volumetric attention, and utilizing a multi-receptive field swin-transformer block, the architecture segments fluid volumes with high precision for three relevant metrics. We provide comparative comparisons with state-of-the-art 3D CNN and Transformer models, where our model supersedes them. Clinical experts can efficiently employ our architecture in various segmentation applications and ophthalmic modalities. The model is best suited for locating inter- and sub-retinal layer fluid deposits for early disease diagnosis and monitoring future prognosis. We hope to extend this work to other ophthalmic modalities.

Acknowledgement

This material is based upon work supported by the **** under Grant No. **** issued through ****.

References

1. Bogunović, H., Venhuizen, F., Klimscha, S., Apostolopoulos, S., Bab-Hadiashar, A., Bagci, U., Beg, M.F., Bekalo, L., Chen, Q., Ciller, C., et al.: Retouch: the retinal oct fluid detection and segmentation benchmark and challenge. *IEEE transactions on medical imaging* **38**(8), 1858–1874 (2019)
2. Bourne, R.R., Stevens, G.A., White, R.A., Smith, J.L., Flaxman, S.R., Price, H., Jonas, J.B., Keeffe, J., Leasher, J., Naidoo, K., et al.: Causes of vision loss worldwide, 1990–2010: a systematic analysis. *The lancet global health* **1**(6), e339–e349 (2013)
3. Chiu, S.J., Allingham, M.J., Mettu, P.S., Cousins, S.W., Izatt, J.A., Farsiu, S.: Kernel regression based segmentation of optical coherence tomography images with diabetic macular edema. *Biomedical optics express* **6**(4), 1172–1194 (2015)
4. Dosovitskiy, A., Beyer, L., Kolesnikov, A., Weissenborn, D., Zhai, X., Unterthiner, T., Dehghani, M., Minderer, M., Heigold, G., Gelly, S., et al.: An image is worth 16x16 words: Transformers for image recognition at scale. In: *International Conference on Learning Representations* (2020)
5. Garvin, M.K., Abramoff, M.D., Kardon, R., Russell, S.R., Wu, X., Sonka, M.: Intraretinal layer segmentation of macular optical coherence tomography images using optimal 3-d graph search. *IEEE transactions on medical imaging* **27**(10), 1495–1505 (2008)
6. Garvin, M.K., Abramoff, M.D., Wu, X., Russell, S.R., Burns, T.L., Sonka, M.: Automated 3-d intraretinal layer segmentation of macular spectral-domain optical coherence tomography images. *IEEE transactions on medical imaging* **28**(9), 1436–1447 (2009)
7. Goatman, K.A.: A reference standard for the measurement of macular oedema. *British journal of ophthalmology* **90**(9), 1197–1202 (2006)
8. Hatamizadeh, A., Nath, V., Tang, Y., Yang, D., Roth, H.R., Xu, D.: Swin unetr: Swin transformers for semantic segmentation of brain tumors in mri images. In: *Brainlesion: Glioma, Multiple Sclerosis, Stroke and Traumatic Brain Injuries: 7th International Workshop, BrainLes 2021, Held in Conjunction with MICCAI 2021, Virtual Event, September 27, 2021, Revised Selected Papers, Part I*. pp. 272–284. Springer (2022)
9. Hatamizadeh, A., Tang, Y., Nath, V., Yang, D., Myronenko, A., Landman, B., Roth, H.R., Xu, D.: Unetr: Transformers for 3d medical image segmentation. In: *Proceedings of the IEEE/CVF winter conference on applications of computer vision*. pp. 574–584 (2022)
10. He, X., Fang, L., Tan, M., Chen, X.: Intra-and inter-slice contrastive learning for point supervised oct fluid segmentation. *Ieee Transactions on Image Processing* **31**, 1870–1881 (2022)
11. Kerfoot, E., Clough, J., Oksuz, I., Lee, J., King, A.P., Schnabel, J.A.: Left-ventricle quantification using residual u-net. In: *Statistical Atlases and Computational Models of the Heart. Atrial Segmentation and LV Quantification Challenges: 9th International Workshop, STACOM 2018, Held in Conjunction with MICCAI 2018, Granada, Spain, September 16, 2018, Revised Selected Papers 9*. pp. 371–380. Springer (2019)
12. Kingma, D.P., Ba, J.: Adam: A method for stochastic optimization. *arXiv preprint arXiv:1412.6980* (2014)
13. Li, M.X., Yu, S.Q., Zhang, W., Zhou, H., Xu, X., Qian, T.W., Wan, Y.J.: Segmentation of retinal fluid based on deep learning: application of three-dimensional fully convolutional neural networks in optical coherence tomography images. *International journal of ophthalmology* **12**(6), 1012 (2019)
14. Lin, T.Y., Goyal, P., Girshick, R., He, K., Dollár, P.: Focal loss for dense object detection. In: *Proceedings of the IEEE international conference on computer vision*. pp. 2980–2988 (2017)
15. Liu, Z., Lin, Y., Cao, Y., Hu, H., Wei, Y., Zhang, Z., Lin, S., Guo, B.: Swin transformer: Hierarchical vision transformer using shifted windows. In: *Proceedings of the IEEE/CVF international conference on computer vision*. pp. 10012–10022 (2021)

16. Ma, D., Lu, D., Chen, S., Heisler, M., Dabiri, S., Lee, S., Lee, H., Ding, G.W., Sarunic, M.V., Beg, M.F.: Lf-unet—a novel anatomical-aware dual-branch cascaded deep neural network for segmentation of retinal layers and fluid from optical coherence tomography images. *Computerized Medical Imaging and Graphics* **94**, 101988 (2021)
17. Nittala, M.G., Konduru, R., Ruiz-Garcia, H., Sadda, S.: Effect of oct volume scan density on thickness measurements in diabetic macular edema. *Eye* **25**(10), 1347–1355 (2011)
18. Oktay, O., Schlemper, J., Le Folgoc, L., Lee, M., Heinrich, M., Misawa, K., Mori, K., McDonagh, S., Hammerla, N.Y., Kainz, B., et al.: Attention u-net: Learning where to look for the pancreas. In: *Medical Imaging with Deep Learning* (2018)
19. Philippi, D., Rothaus, K., Castelli, M.: A vision transformer architecture for the automated segmentation of retinal lesions in spectral domain optical coherence tomography images. *Scientific Reports* **13**(1), 517 (2023)
20. Quellec, G., Lee, K., Dolejsi, M., Garvin, M.K., Abramoff, M.D., Sonka, M.: Three-dimensional analysis of retinal layer texture: identification of fluid-filled regions in sd-oct of the macula. *IEEE transactions on medical imaging* **29**(6), 1321–1330 (2010)
21. Roy, A.G., Conjeti, S., Karri, S.P.K., Sheet, D., Katouzian, A., Wachinger, C., Navab, N.: Relaynet: retinal layer and fluid segmentation of macular optical coherence tomography using fully convolutional networks. *Biomedical optics express* **8**(8), 3627–3642 (2017)
22. Schlegl, T., Waldstein, S.M., Bogunovic, H., Endstraßer, F., Sadeghipour, A., Philip, A.M., Podkowinski, D., Gerendas, B.S., Langs, G., Schmidt-Erfurth, U.: Fully automated detection and quantification of macular fluid in oct using deep learning. *Ophthalmology* **125**(4), 549–558 (2018)
23. Srinivasan, P.P., Kim, L.A., Mettu, P.S., Cousins, S.W., Comer, G.M., Izatt, J.A., Farsiu, S.: Fully automated detection of diabetic macular edema and dry age-related macular degeneration from optical coherence tomography images. *Biomedical optics express* **5**(10), 3568–3577 (2014)
24. Tang, Y., Yang, D., Li, W., Roth, H.R., Landman, B., Xu, D., Nath, V., Hatamizadeh, A.: Self-supervised pre-training of swin transformers for 3d medical image analysis. In: *Proceedings of the IEEE/CVF Conference on Computer Vision and Pattern Recognition*. pp. 20730–20740 (2022)
25. Ting, D.S.W., Cheung, G.C.M., Wong, T.Y.: Diabetic retinopathy: global prevalence, major risk factors, screening practices and public health challenges: a review. *Clinical & experimental ophthalmology* **44**(4), 260–277 (2016)
26. Tranos, P.G., Wickremasinghe, S.S., Stangos, N.T., Topouzis, F., Tsinopoulos, I., Pavesio, C.E.: Macular edema. *Survey of ophthalmology* **49**(5), 470–490 (2004)
27. Wang, M., Yu, K., Xu, X., Zhou, Y., Peng, Y., Xu, Y., Goh, R.S.M., Liu, Y., Fu, H.: Tiny-lesion segmentation in oct via multi-scale wavelet enhanced transformer. In: *Ophthalmic Medical Image Analysis: 9th International Workshop, OMIA 2022, Held in Conjunction with MICCAI 2022, Singapore, Singapore, September 22, 2022, Proceedings*. pp. 125–134. Springer (2022)
28. Wong, W.L., Su, X., Li, X., Cheung, C.M.G., Klein, R., Cheng, C.Y., Wong, T.Y.: Global prevalence of age-related macular degeneration and disease burden projection for 2020 and 2040: a systematic review and meta-analysis. *The Lancet Global Health* **2**(2), e106–e116 (2014)
29. Xing, G., Chen, L., Wang, H., Zhang, J., Sun, D., Xu, F., Lei, J., Xu, X.: Multi-scale pathological fluid segmentation in oct with a novel curvature loss in convolutional neural network. *IEEE Transactions on Medical Imaging* **41**(6), 1547–1559 (2022)
30. Yang, J., Ji, Z., Niu, S., Chen, Q., Yuan, S., Fan, W.: Rmppnet: residual multiple pyramid pooling network for subretinal fluid segmentation in sd-oct images. *OSA Continuum* **3**(7), 1751–1769 (2020)